1

Application of Mössbauer Spectroscopy to Energy Materials

Pierre-Emmanuel Lippens, Jean-Claude Jumas, and Josette Olivier-Fourcade

Institut Charles Gerhardt de Montpellier, UMR 5253 CNRS, Université de Montpellier, ENSCM,
Pôle Chimie Balard Recherche 1919 route de Mende, Montpellier Cedex 5, France

1.1 Introduction

The increasing demand for energy and the environmental problems caused by fossil fuels make necessary the fast development of renewable and clean energy sources such as solar or wind. However, their intermittent nature requires highly efficient energy storage systems. Furthermore, clean transportation, such as electric or hybrid vehicles, needs power sources of high energy density. In this regard, lithium-ion batteries can be considered as one of the most promising technologies. Although lithium-ion batteries are used in electronic devices, power tools, electric bikes, and more, there are still many challenges to overcome for new applications that require higher energy and power densities, improved safety, and lower cost. This explains the current intensive research on electrode materials [1, 2].

The performance of currently used carbon and layered lithium transition metal oxides as negative and positive electrode materials, respectively, has almost reached the upper theoretical limits. New negative electrode materials such as silicon and tin have high theoretical capacities, but they suffer from strong volume variations during cycling, which leads to capacity fading and strongly reduces the cycle life [3, 4]. Among the different approaches proposed to improve the performance of such materials, downsizing the particle size or dispersing particles within an electrochemically inactive matrix have been proposed [5, 6]. For the positive electrodes, new Fe-containing materials such as $LiFePO_4$, $LiFe_{1-x}Mn_xPO_4$, or $LiFePO_4F$ appear to be very promising for environmental and economic aspects [7, 8]. Finally, the potential problems of cobalt and lithium supply in a near future have recently led to the development of alternative technologies such as Na-ion batteries [9, 10].

Improving the performance of electrode materials requires a good knowledge of the electrochemical reaction mechanisms in batteries. Mössbauer spectroscopy is often used for the characterization of materials, but is also a unique tool to follow such reactions at the atomic scale from the analysis of the Mössbauer parameters: isomer shift (given in this chapter relative to α-Fe and $BaSnO_3$ for

[57]Fe and [119]Sn isotopes, respectively), quadrupole splitting and hyperfine magnetic field [11, 12]. Different examples are considered to illustrate the application of Mössbauer spectroscopy to electrode materials for Li-ion and Na-ion batteries. This includes tin-based negative electrode materials: β-Sn, tin oxides, tin borophosphates, tin intermetallics, and tin-silicon composites, as well as iron-based positive electrode materials: $LiFePO_4$, $LiFe_{1-x}Mn_xPO_4$, $Fe_{1.19}PO_4(OH)_{0.57}(H_2O)_{0.43}$, and $Na_{1.5}Fe_{0.5}Ti_{1.5}(PO_4)_3$.

Reducing emission and pollution of existing transportation based on fossil fuels is also a great challenge. Reforming catalysis is a major petroleum refining process for the production of hydrogen or high-octane gasoline. In particular, catalytic reforming is a chemical process used to convert naphtha, produced during petroleum refining, into high-octane number gasoline. If Pt/Al_2O_3 was the first naphtha-reforming catalyst, a great progress has been achieved with supported bimetallic-reforming catalysts, in which Pt is promoted by another metal such as Sn, that offer high selectivity at low pressure [13]. Improved selectivity can be obtained by the addition of a second promoter as In [14]. Mössbauer spectroscopy has been widely used in catalysis [15, 16]. Some examples are presented here to show how complex redox processes in Sn-Pt based catalysts involving many different tin species can be elucidated.

1.2 Mössbauer Spectroscopy for Li-ion and Na-ion Batteries

1.2.1 Characterization of Electrode Materials and Electrochemical Reactions

The main specifications of electrode materials for Li-ion or Na-ion batteries are specific and volumetric capacities, nominal potential, cycle life, calendar life, rate capability, safety, environmental impact, and recycling. It is of course impossible to optimize all these features at the same time. For example, layered lithium transition metal oxides, as commonly used positive electrode materials for Li-ion batteries, have high capacity and high potential vs. Li^+/Li. Lithium iron phosphate ($LiFePO_4$) has lower capacity but provides better safety and higher electric power. Thus, new electrode materials are needed to improve the performance of Li-ion and Na-ion batteries. This requires a better knowledge of the electrochemical reaction mechanisms that take place during the charge–discharge cycles.

Different techniques have been used for the characterization of electrode materials and to follow the reactions within the batteries. This includes ex situ experiments, i.e. the electrode material is extracted from the battery, in situ experiments, i.e. the electrode material is in the battery, and operando experiments as electrochemical reactions proceed [17]. X-ray diffraction (XRD) and Mössbauer spectroscopy have often been combined to obtain complementary information about long range and local properties, respectively [18]. It is thus possible to determine the formed species even if they are amorphous, to follow changes in local structure or oxidation state in order to elucidate the reaction mechanisms.

In situ and operando Mössbauer and XRD measurements require specific electrochemical cells that allow transmission of γ-rays and reflection of X-rays,

respectively, while voltage or electric current is imposed. Such a cell is based on the usual positive electrode/separator/electrolyte/negative electrode configuration [19, 20]. To investigate the electrochemical reactions for a given electrode material, a half-cell is commonly used, where the negative electrode is metallic lithium (or sodium) and the positive electrode is the formulated electrode material under investigation. The formulation consists of mixing the electrochemically active material (nanoparticles or microparticles) with an electronic conductive additive, like carbon black, and a binder to form a slurry that is casted onto the metal current collector [21]. In the case of an electrochemical half-cell, the discharge corresponds to the lithiation (or sodiation) of the electrode material under investigation and the charge to delithiation (or desodiation).

1.2.2 Tin-Based Negative Electrode Materials for Li-ion Batteries

1.2.2.1 Electrochemical Reactions of Lithium with Tin

Metallic and semi-metallic elements can be used as negative electrode materials for high energy Li-ion batteries. For example, each Sn atom in β-Sn can react with a maximum of 4.4 Li, which corresponds to specific and volumetric capacities of 992 mAh·g^{-1} and 2111 mAh·cm^{-3}, respectively [3]. This is more than 2.6 times the capacity of currently used graphite (372 mAh·g^{-1} and 719 mAh·cm^{-3}). In addition, the average potential of β-Sn in a Li half-cell is higher than that of carbon, which reduces lithium plating and improves safety. Unfortunately, the formation of $Li_{x<4.4}Sn$ phases during lithiation induces a strong increase of the particle volume (>300%) that causes cracks, while delithiation leads to the pulverization of the particles. These two effects are responsible for mechanical and electrical instabilities of the negative electrode film, which drastically reduces the cycle life of the battery. XRD and ^{119}Sn Mössbauer spectroscopy have been combined to obtain deeper insights into Li–Sn alloying reactions.

The experimental voltage curves of β-Sn in a Li half-cell, obtained during the first cycle in galvanostatic regime at low current density, show different well-defined plateaus that can be attributed to two-phase reactions (Figure 1.1) [22].

The voltage plateaus are observed for both lithiation and delithiation processes, showing the reversibility of the mechanism. The following alloying reactions have been proposed by considering the different crystalline phases of the commonly accepted Li–Sn phase diagram [24]:

$$5 \, \beta\text{-Sn} + 2 \, \text{Li} \rightarrow \text{Li}_2\text{Sn}_5 \tag{1.1}$$

$$\text{Li}_2\text{Sn}_5 + 3 \, \text{Li} \rightarrow 5 \, \text{LiSn} \tag{1.2}$$

$$3 \, \text{LiSn} + 4 \, \text{Li} \rightarrow \text{Li}_7\text{Sn}_3 \tag{1.3}$$

$$2 \, \text{Li}_7\text{Sn}_3 + \text{Li} \rightarrow 3 \, \text{Li}_5\text{Sn}_2 \tag{1.4}$$

$$5 \, \text{Li}_5\text{Sn}_2 + \text{Li} \rightarrow 2 \, \text{Li}_{13}\text{Sn}_5 \tag{1.5}$$

$$2 \, \text{Li}_{13}\text{Sn}_5 + 9 \, \text{Li} \rightarrow 5 \, \text{Li}_7\text{Sn}_2 \tag{1.6}$$

$$5 \, \text{Li}_7\text{Sn}_2 + 9 \, \text{Li} \rightarrow 2 \, \text{Li}_{22}\text{Sn}_5 \tag{1.7}$$

First-principles calculations of the cell voltage were performed with different methods based on density functional theory (DFT) for reactions (1.1)–(1.6) [22, 23].
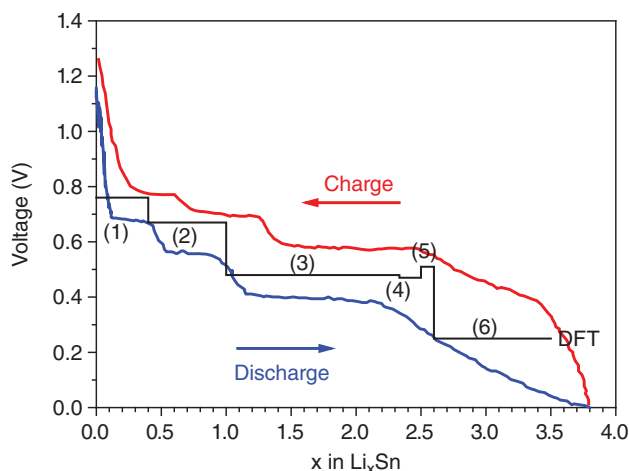
Figure 1.1 Experimental voltage profile for the first cycle of β-Sn in Li half-cell [22] and voltage plateaus evaluated with density functional theory (DFT) for the reactions (1.1)–(1.6) described in the text [23]. Source: Adapted from Refs. [22, 23].

The comparison between the experimental and theoretical voltage profiles suggests that the two first plateaus at average experimental voltages of 0.75 V and 0.65 V reflect the formation of Li_2Sn_5 (reaction 1.1) and LiSn (reaction 1.2) crystalline phases, respectively. The following plateau, at about 0.5 V, could be attributed to the formation of Li_7Sn_3 (reaction 1.3), Li_5Sn_2 (reaction 1.4), and/or $Li_{13}Sn_5$ (reaction 1.5) that have closed chemical compositions and formation energies. The expected plateau for the formation of Li_7Sn_2 (reaction 1.6) is not observed experimentally since the voltage curve shows a continuous decrease in the range 2.2–3.8 Li per Sn. This was interpreted by the formation of a metastable phase with a body-centered cubic disordered structure showing the same short-range order as $Li_{22}Sn_5$ [22].

Operando XRD was used to follow the structural changes of β-Sn small particles in Li half-cell during the first cycle in galvanostatic regime (Figure 1.2).

During the discharge, the successive XRD patterns show the main peaks of β-Sn, Li_2Sn_5, and LiSn, confirming that the two first voltage plateaus correspond to the reactions (1.1) and (1.2). Then, there is one broad band around $2\theta = 25°$ and a peak at $2\theta = 45°$ that can be attributed to one or more Li-rich Li_xSn phases, but it is not possible to determine the chemical composition from the XRD patterns. The large linewidth and the small intensity of the peaks indicate that the electrochemically formed Li_xSn phases are poorly crystallized and/or of small size. The nanostructuration of the pristine material is typical of alloying reactions and explains the inability of XRD to give accurate information about such electrochemical mechanisms, especially for the highly lithiated electrodes. The mechanism is clearly reversible during the charge, but it is still difficult to distinguish all the intermediate Li_xSn phases. In such a case, [119]Sn Mössbauer spectroscopy is of particular interest since it is sensitive to the local environment of the Sn atoms and not to long-range order.
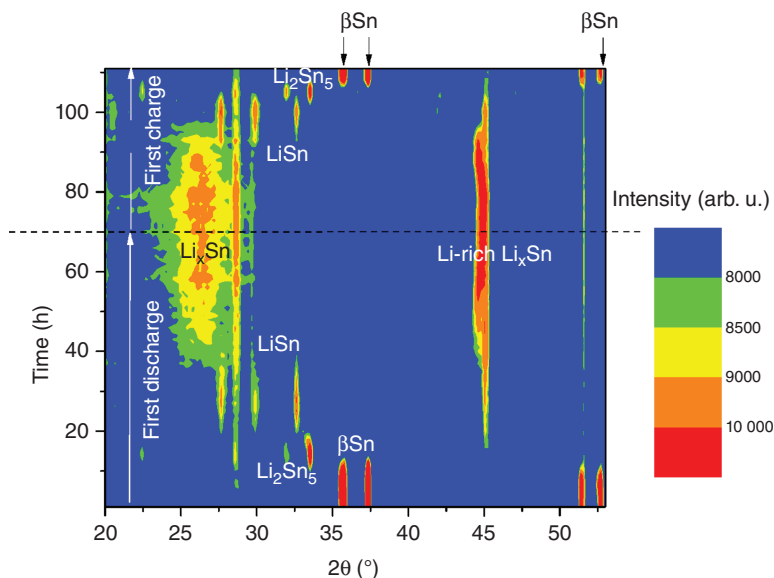
Figure 1.2 Operando XRD patterns obtained during the first discharge and the first charge of β-Sn in Li half-cell (galvanostatic regime) where colors reflect X-ray intensity.

To have some reference compounds that can help in the interpretation of the [119]Sn Mössbauer experiments during the charge–discharge reactions, the spectra of the seven Li_xSn crystalline phases, Li_2Sn_5, LiSn, Li_7Sn_3, Li_5Sn_2, $Li_{13}Sn_5$, Li_7Sn_2 and $Li_{22}Sn_5$, were measured at room temperature [24]. These phases were obtained in two different ways, namely high temperature solid-state reactions [25] and mechanosynthesis followed by annealing [26]. The crystal structures determined by XRD show the existence of one (Li_5Sn_2), two (Li_2Sn_5, LiSn, Li_7Sn_2), three (Li_7Sn_3, $Li_{13}Sn_5$), and four ($Li_{22}Sn_5$) crystallographic sites for Sn. The Mössbauer spectra obtained for the two series of synthesized materials give similar Mössbauer parameters. The observed small differences are due to the existence of impurities and the difficulties to fit unresolved spectra. One set of spectra and the corresponding parameters are reported in Figure 1.3 and Table 1.1, respectively.

The values of the quadrupole splitting, Δ, can be related to the different local environments of Sn resulting from the existence of different types of nearest neighbors (Li, Sn), polyhedral geometries, and bond lengths [26]. The average value of the isomer shift, δ_{av}, is of about 2.4 mm·s^{-1} for the two Sn-rich phases and decreases from 2.1 to 1.8 mm·s^{-1} with increasing number of Li per Sn for the Li-rich phases. These values are typical of the Sn(0) oxidation state. They reflect the existence of a Sn based sublattice for the Sn-rich phases and the decrease in the number of Sn—Sn bonds per Sn for the Li-rich phases.

The values of δ_{av} are plotted for the Li_xSn references as a function of x (Figure 1.4). The linear correlation shows that $\delta_{av}(x)$ mainly depends on the average chemical composition of Li_xSn and can be used to evaluate x for amorphous phases or small particles as often encountered in electrochemical reactions. The linear function
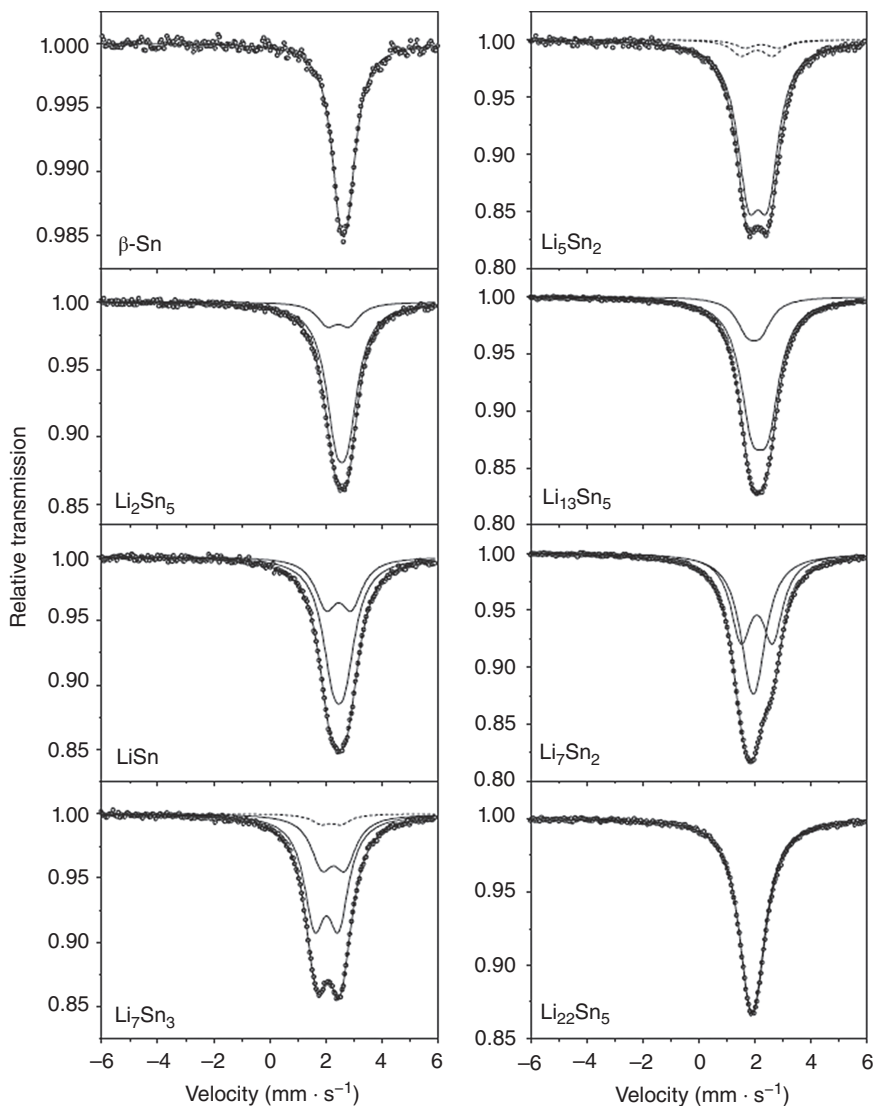
Figure 1.3 ^{119}Sn Mössbauer spectra of Li$_x$Sn crystalline phases measured at room temperature. Source: Reproduced from Ref. [26]/with permission from Elsevier.

obtained for the regression line shown in Figure 1.4 can be written as:

$$\delta_{av}(\text{mm} \cdot \text{s}^{-1}) = 2.55 - 0.20x \tag{1.8}$$

Other empirical correlation rules have been derived from the Li$_x$Sn Mössbauer references, such as δ–Δ correlation diagrams used to predict the electrochemical activity of Sn based negative electrode materials for Li-ion batteries (Figure 1.5) [27].

The ^{119}Sn Mössbauer spectroscopy was used for ex situ measurements at different stages of the first discharge of β-Sn in Li half-cells [28]. The shape of the voltage curve

Table 1.1 Values of the [119]Sn Mössbauer parameters of Li$_x$Sn crystalline phases obtained by Robert et al. [26]. The values of the isomer shift, δ, relative to BaSnO$_3$ and quadrupole splitting, Δ, are reported for Sn in different crystallographic sites.

	β-Sn	Li$_2$Sn$_5$	LiSn	Li$_7$Sn$_3$	Li$_5$Sn$_2$	Li$_{13}$Sn$_5$	Li$_7$Sn$_2$	Li$_{22}$Sn$_5$
δ/Δ (mm·s⁻¹) (crystallographic sites)	2.56/0.29 (4a)	2.49/042 (8i) 2.36/0.78 (2d)	2.38/0.43 (2m) 2.38/0.91 (1a)	2.19/0.82 (2e) 1.94/0.86 (2e, 2e)	2.01/0.69 (6c)	1.86/0.48 (1a) 2.07/0.58 (2d, 2d)	1.84/0.28 (4i) 1.96/1.13 (4h)	1.83/0.31 (16e, 16e, 24f, 24g)

Source: Adapted from Ref. [26].

Figure 1.4 Average experimental values of the isomer shift of the Li$_x$Sn crystalline references vs. number of Li per Sn and linear regression line (blue).

is similar to that of Figure 1.1, except at the very beginning of lithiation due to the existence of tin oxides as impurities. The spectra recorded for the insertion of 0.5, 1, and 3.4 Li per Sn were fitted to two doublets and the values of the Mössbauer parameters are similar to those of Li$_2$Sn$_5$, LiSn, and Li$_7$Sn$_2$ references, respectively, although there are some small differences that can be attributed to the poor crystallinity and to variations in the chemical composition of the electrochemically lithiated species.

Although β-Sn has a higher capacity than graphite, it suffers from large volume variations during cycling that affect the mechanical and electrical integrity of the electrode film. Tin oxide composites were proposed to reduce such effects [29], and the electrochemical mechanisms are described in the following two paragraphs by considering the application of Mössbauer spectroscopy.

1.2.2.2 Tin Oxides

Stannic oxide (SnO$_2$) and stannous oxide (SnO) have tetragonal *P*4$_2$/*mnm* and *P*4/*nmm* structures, respectively. The Mössbauer spectrum of SnO$_2$ is formed by
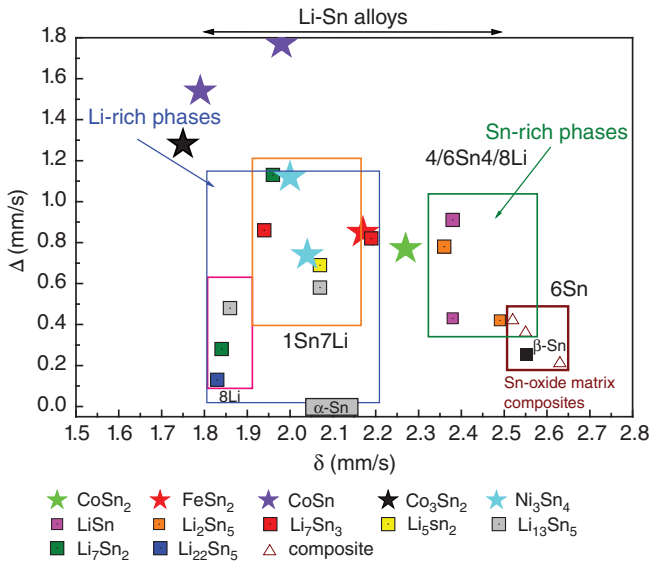
Figure 1.5 Correlation diagram for Sn-based materials based on experimental values of isomer shift, δ, and quadrupole splitting, Δ.

a single peak reflecting the Sn(IV) oxidation state ($\delta = 0\,\text{mm·s}^{-1}$) and a slightly distorted SnO_6 octahedral environment ($\Delta = 0.5\,\text{mm·s}^{-1}$). SnO can be described as parallel Sn–O–Sn layers, and each Sn atom is bonded to four O atoms to form a SnO_4 square based pyramid. The Mössbauer spectrum consists of an asymmetric doublet characteristic of the Sn(II) oxidation state ($\delta = 2.63\,\text{mm·s}^{-1}$), while the quadrupole splitting ($\Delta = 1.33\,\text{mm·s}^{-1}$) reflects the anisotropy of the Sn p-type electron density arising from the Sn 5p lone pair along the fourfold pyramid axis.

The voltage profiles of SnO_2 and SnO based electrodes obtained in galvanostatic regime show similar trends [30–33]. The first discharge of SnO is formed by a plateau at ~1 V for 2 Li per Sn (Region R1), followed by a continuous voltage decrease showing different pseudo-plateaus (Region R2) (Figure 1.6). Then, the voltage profiles of the two tin oxides are similar to that of β-Sn for the subsequent charge–discharge cycles. The electrochemical mechanism was studied by ex situ [31] and operando [32] [119]Sn Mössbauer spectroscopy. As lithiation proceeds in R1, there is a progressive broadening of the spectra at the low velocity side, ending with a large and unresolved peak at the end of the first plateau (A–D in Figure 1.7). The experimental spectra were successfully fitted to three components corresponding to SnO, β-Sn, and a Sn(IV) oxide, respectively, and an additional component centered at about $1.2\,\text{mm·s}^{-1}$. The contribution of SnO decreases during the lithiation while that of β-Sn increases, which corresponds to the conversion reaction:

$$SnO + 2\,Li \rightarrow \beta\text{-}Sn + Li_2O \tag{1.9}$$

The subspectrum at $1.2\,\text{mm·s}^{-1}$ can been attributed to Sn bonded to both Sn and O atoms resulting from interactions between β-Sn and Li_2O small particles or to the existence of Li–Sn–O amorphous phases. In region R2, the ex situ spectra E and F
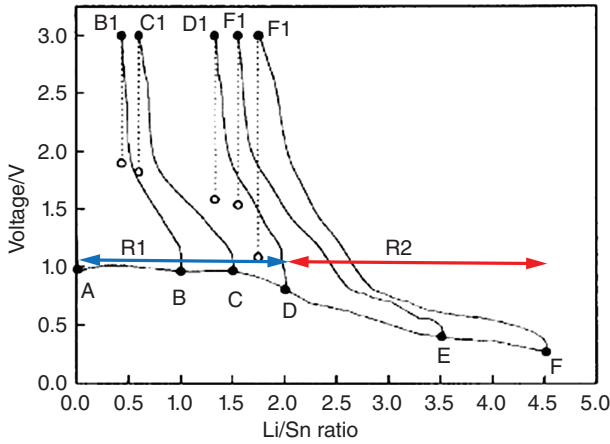
Figure 1.6 Voltage curves of SnO in Li half-cell with the points of measurements for the first discharge (A–F) and full charges at 3 V (B1–F1). Source: Reproduced from Ref. [31]/with permission from Elsevier.

Figure 1.7 Ex situ ^{119}Sn Mössbauer spectra at different stages of the first discharge and of the end of charges. Source: Reproduced from Ref. [31]/with permission from Elsevier.
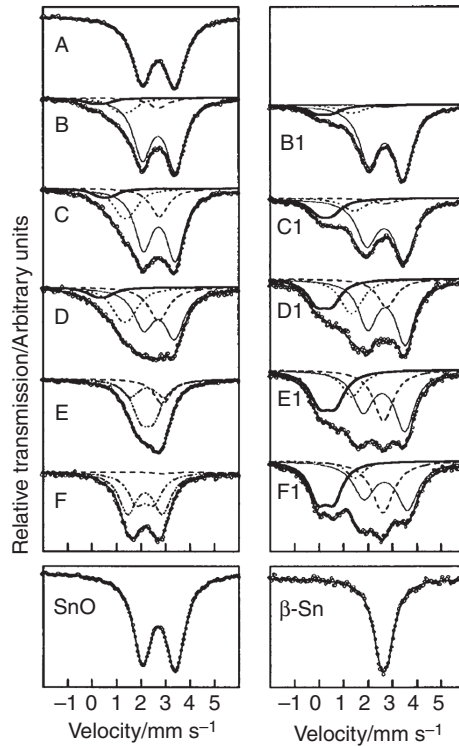
(Figure 1.7) are similar to published in situ Mössbauer spectra [32]. However, more spectra were recorded in the latter case due to a deeper lithiation. They are close to the spectra of the reference materials, confirming the formation of Sn-rich and Li-rich Li_xSn equilibrium phases, except around Li_5Sn_2 as discussed above for β-Sn. The Li_xSn dealloying reactions operate during the charge, but a back reaction of Sn with O, arising from the delithiation of Li_2O, is observed at high voltage. The later reaction is out of the usual voltage range for negative electrodes in Li-ion batteries and should not be considered. In that case, the electrochemical mechanism of SnO consists of the irreversible conversion reaction of Sn(II)O into β-Sn(0) followed by reversible Li_xSn alloying reactions. The Li_2O particles form an electrochemically inactive matrix that maintains the dispersion of the Li_xSn particles and buffers the volume variations, improving the cycling behavior compared to β-Sn. However, the in situ formation of the Li_2O matrix leads to a capacity loss at the first cycle that requires a compensation by the lithiated positive electrode in a Li-ion full-cell. The situation is even more critical for SnO_2 since four Li per Sn are required for its transformation into β-Sn/Li_2O nanocomposite.

1.2.2.3 Tin Borophosphates

Tin composite oxides (TCO) were proposed by Fuji in the late 1990s as negative electrode materials for Li-ion batteries [29]. Among the different TCOs, the tin borophosphate glass $SnO(B_2O_3)_{0.25}(P_2O_5)_{0.25}$ (Sn_2BPO_6 in the text) was studied by in situ ^{119}Sn Mössbauer spectroscopy [32]. The voltage profile of the first cycle of Sn_2BPO_6 in a Li half-cell is similar to that of SnO, except that the voltage of the first plateau (1.75 V) is higher (Figure 1.8). The Mössbauer spectrum of $Sn(II)_2BPO_6$, similar to that of SnO, is transformed into a broad band of weak intensity at the end of the first plateau. This reflects the transformation of the Sn(II) based pristine material into β-Sn small clusters embedded in a mixed borophosphate and lithium oxide matrix (Figure 1.8). Then, the Mössbauer spectra are similar to the Li_xSn references except around Li_5Sn_2. The spectra obtained along the first charge until 1 V were attributed to the Li_xSn phases resulting from dealloying reactions, which is consistent with a reversible process. As the charge proceeds until 2.5 V, there is a partial reformation of Sn_2BPO_6.

Thus, the electrochemical mechanism of Sn_2BPO_6 glass consists in the formation of Sn(0) tiny particles embedded in a more complex matrix than that obtained for SnO, followed by alloying–dealloying Li_xSn reactions. The value of the voltage cutoff for charge (≈0.8 V) is crucial to avoid back reaction of Sn with O. The electrochemical performance of TCO, such as cyclability, shows that a borophosphate matrix is more efficient than a Li_2O matrix, as obtained for tin oxide compounds, to maintain the dispersion of the Li_xSn particles and buffer the volume variations during cycling.

Tin borophosphate composites were also considered as possible negative electrode materials for Li-ion batteries, such as $Sn/(BPO_4)_{0.2}$ that shows a reversible capacity of about 500 mAh·g^{-1} [33, 34]. The operando Mössbauer measurements were performed in galvanostatic regime at C/10 in the voltage range 0.1–1.2 V [35]. The Mössbauer spectrum of the pristine material shows the existence of β-Sn but also of an amorphous Sn(II)-borophosphate phase not observed by XRD

Figure 1.8 In situ ^{119}Sn Mössbauer spectra at different stages of the first discharge of Sn_2BPO_6. Source: Reproduced from Ref. [32]/with permission from Elsevier.
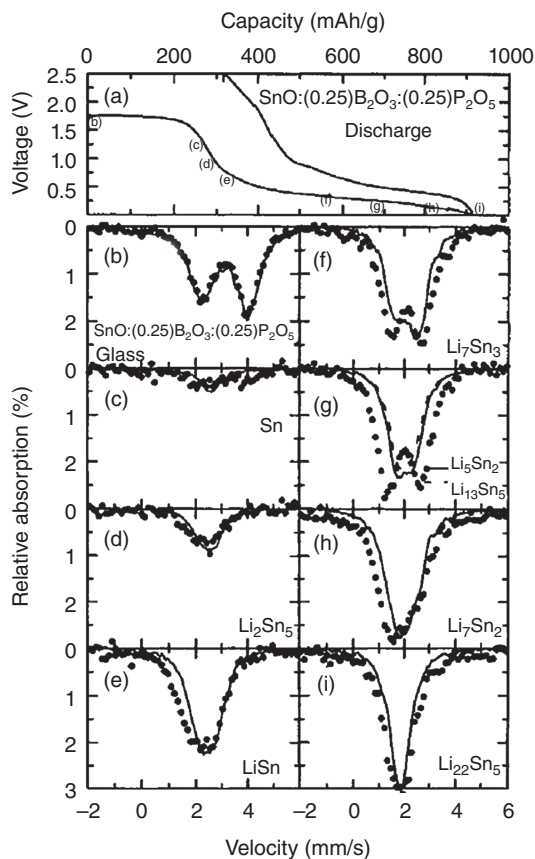
(Figure 1.9). At the beginning of discharge, the voltage curve shows a plateau at 1.5 V, significantly shorter than the plateaus of tin oxides or TCO discussed above, followed by a voltage decrease until 0.4 V for about 0.6 Li per Sn (Figure 1.10a). The intensity of the Sn(II) Mössbauer absorption strongly decreases in the range 0–0.2 Li per Sn, which indicates that the plateau corresponds to the reduction of the Sn(II) amorphous phase into Sn(0) (Figure 1.10b). Then, there is no more change in the spectra until 0.9 V, in line with the irreversible reaction of lithium with the electrolyte, leading to the formation of a solid electrolyte interphase (SEI) at the particle surface. As discharge proceeds further, the voltage curve shows a plateau at 0.4 V and then decreases until 0.1 V in the range from 0.6 to 3.2 Li per Sn. The average Mössbauer isomer shift decreases from 2.45 to 2.0 mm·s^{-1}. By considering the $\delta_{av}(x)$ linear function for Li_xSn (see Eq. 1.8), the latter value suggests that $x \approx 2.5$ (Figure 1.10c and 1.10d), in agreement with the 2.6 Li reacting with β-Sn in this region. This low value of x, compared to the expected $Li_{22}Sn_5$ phase, is due to the voltage cutoff of 0.1 V used in this experiment, which prevents deep lithiation. During the first charge, the average isomer shift linearly increases, as expected from the delithiation of Li_xSn, ending with $\delta_{av} \approx 2.35$ mm·s^{-1}, which corresponds to $x \approx 1$. This confirms the reversibility of the alloying process although
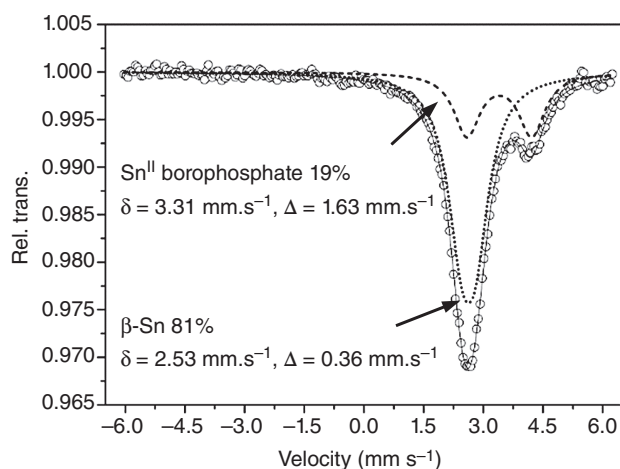
Figure 1.9 ^{119}Sn Mössbauer spectrum of Sn/(BPO$_4$)$_{0.2}$ composite (relative transmission: rel. trans.) showing the relative amounts of Sn^{II} and Sn^0 species. Source: Adapted from Ref. [35].
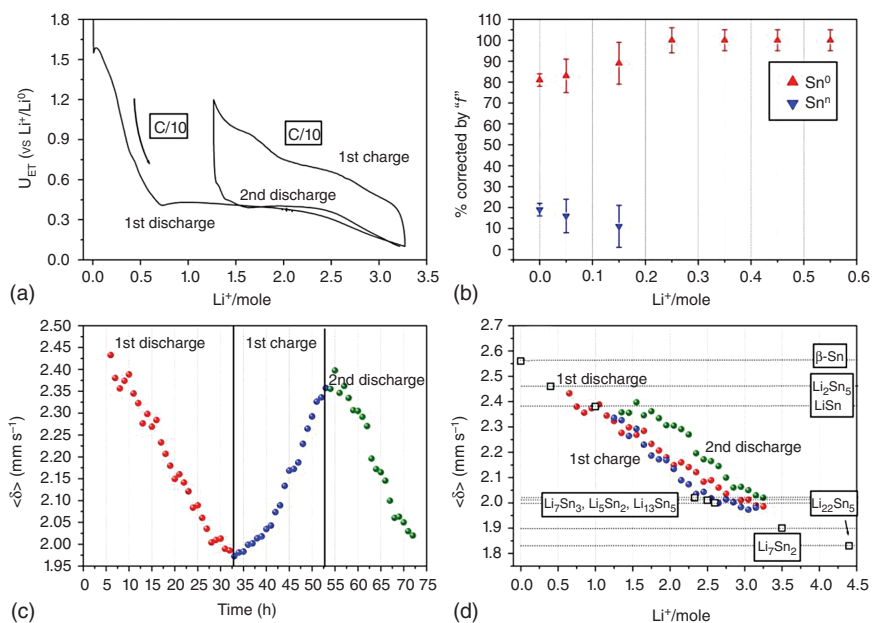

Figure 1.10 Voltage profile of Sn/(BPO$_4$)$_{0.2}$ in Li half-cell for the galvanostatic regime of C/10 (a), amounts of Sn(II) and Sn(0) at the beginning of first discharge (b), evolution of the Sn(0) average isomer shift, δ, as a function of time reaction (c), and as a function of the number of Li per Sn (d): first discharge in red, first charge in blue, and second discharge in green.

there is no full delithiation. The voltage profile observed for the second discharge is similar to the first one but is in the range 1.3–3.2 Li per Sn. The average isomer shift follows the same trend as during the first discharge, corresponding to the progressive change in the average composition of Li_xSn from x = 1 to about 2.5.

The results reported here for tin oxides as negative electrode materials for Li-ion batteries show that the first discharge consists in the restructuration of the electrode material, ending with Li-rich Li_xSn nanoparticles dispersed in an electrochemically inactive matrix composed of oxide, borate, or phosphate based particles. This matrix helps to buffer the strong volume variations of Li_xSn during alloying–dealloying reactions, reducing the capacity fading and improving the cycle life. However, there are still some issues regarding the capacity loss at first cycle due to the irreversible consumption of Li and the large voltage polarization due to the poor electronic conductivity of the oxide based matrix. Significant improvements have been obtained with tin intermetallics as described in the following section.

1.2.2.4 Tin-Based Intermetallics

Advantages over Tin Oxides The use of tin intermetallics as negative electrode materials for Li-ion batteries is based on the same concept as tin oxides, which is to form a nanocomposite during the first discharge, except that the matrix is composed of metallic particles in order to improve the electronic conductivity. In addition, the microstructure of metal based matrices is different from that of oxide matrices, which could be advantageous for buffering the volume changes resulting from Li_xSn alloying reactions. But the most interesting aspect of tin intermetallics is the existence of Sn(0) oxidation state. There is no reduction of tin prior to alloying lithiation during the first discharge, as Sn(IV) or Sn(II) in tin oxides, which reduces the capacity loss of the first cycle. Most of the tin-based intermetallics, MSn_x, combine Sn with a transition metal, M, that does not react with Li. The first discharge is expected to extrude the M atoms from MSn_x to form metallic nanoparticles (the matrix) that maintain the dispersion of Li_xSn nanoparticles. Although carbon additives and a binder are added to MSn_x particles to form the conductive film casted on the metal current collector, carbon can also be introduced during the synthesis process to form a MSn_x/C composite. Such composites have been widely studied in relation with the commercialization by Sony of the Nexelion Li-ion batteries [36–40]. The specific capacity was about twice as high than that of graphite. A detailed study of $FeSn_2$ is presented in the following part. This compound is of particular interest to follow lithiation–delithiation reactions since it contains both ^{57}Fe and ^{119}Sn Mössbauer isotopes.

Electrochemical Reactions of Lithium with FeSn₂ $FeSn_2$ has a tetragonal structure ($I4/mcm$), and the unit cell contains one crystallographic site for Fe at the center of a Sn based square antiprism. There is also one crystallographic site for Sn bonded to four Fe atoms to form a $SnFe_4$ square based pyramid. $FeSn_2$ microparticles were synthesized by solid-state reaction as electrode material for Li-ion batteries and nanostructured by an additional ball-milling step [41]. The $FeSn_2$ crystal is antiferromagnetic below 378 K [42], and the ^{57}Fe Mössbauer spectrum is formed
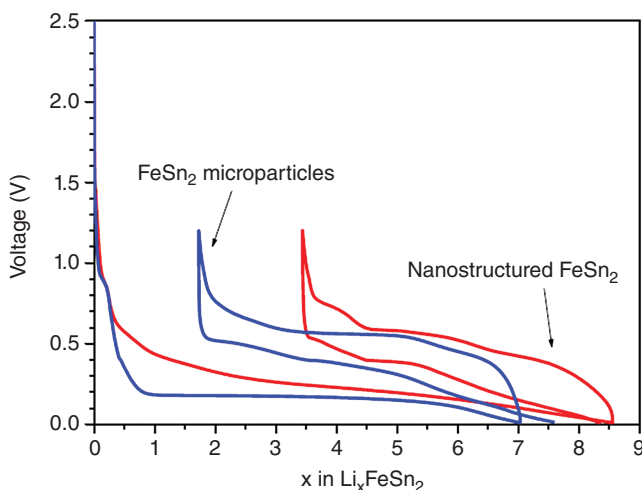
Figure 1.11 Voltage profiles of FeSn$_2$ based electrodes at C/50. Source: Reproduced from Ref. [41]/with permission from Elsevier.

by a sextet at room temperature. The ^{119}Sn Mössbauer spectrum shows broad structures in the range 0–5 mm·s^{-1}, reflecting a transferred hyperfine magnetic field [43]. The Mössbauer parameters: $\delta = 0.5$ mm·s^{-1}, $\Delta = 0$ mm·s^{-1}, B = 11 T for Fe and $\delta = 2.18$ mm·s^{-1}, $\Delta = 0.83$ mm·s^{-1}, B = 2.4 T for Sn are typical of Fe(0) and Sn(0) oxidation states with a Sn asymmetrical environment. Similar values of the Mössbauer parameters were obtained for nanostructured FeSn$_2$ except there is no hyperfine magnetic field because of the small size and the poor crystallinity of the FeSn$_2$ ground particles [41].

The voltage profile of the electrode containing FeSn$_2$ microparticles shows a low voltage plateau for the first discharge and a voltage hysteresis at the average value of 0.5 V for the following cycles (Figure 1.11). The voltage curve of the first discharge differs from that of tin oxides and reflects a two-phase reaction. This is confirmed by operando XRD that shows the direct transformation of FeSn$_2$ into a Li-rich Li$_x$Sn phase as lithiation proceeds. However, the chemical composition and the structure of the formed Li$_x$Sn phase cannot be determined due to unresolved Bragg peaks. The operando ^{119}Sn Mössbauer spectra show strong changes from the magnetic spectrum of FeSn$_2$ to an asymmetrical peak at the end of discharge (Figure 1.12a). The Mössbauer parameters of the fully lithiated electrode are close to those of the Li$_7$Sn$_2$ crystalline reference except for one value of the quadrupole splitting ($\Delta = 0.72$ mm·s^{-1}) smaller than the reference ($\Delta = 1.13$ mm·s^{-1}). This was attributed to the small size and/or poor crystallinity of the Li$_7$Sn$_2$ particles [44]. The ^{57}Fe Mössbauer spectra change from a sextet for FeSn$_2$ to a doublet with Mössbauer parameters ($\delta = 0.2$ mm·s^{-1}, $\Delta = 0.5$ mm·s^{-1}) that can be attributed to α-Fe nanoparticles in paramagnetic state (Figure 1.12b).

All the intermediate ^{57}Fe and ^{119}Sn Mössbauer spectra were successfully fitted to the spectra of FeSn$_2$/α-Fe(nano) and FeSn$_2$/Li$_7$Sn$_2$(nano) phases, respectively, showing that the first discharge can be described by the two-phase reaction:

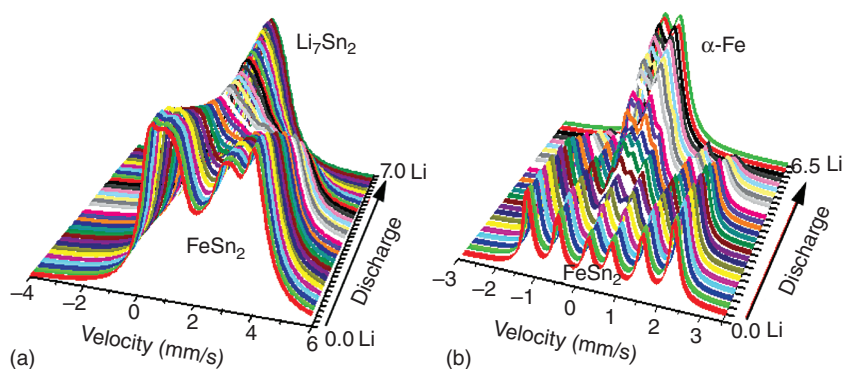$$FeSn_2 + 7\,Li \rightarrow Li_7Sn_2 + Fe \tag{1.10}$$

Figure 1.12 Operando ^{119}Sn (a) and ^{57}Fe (b) Mössbauer spectra obtained during the first galvanostatic discharge of $FeSn_2$ (microparticles) electrode in Li half-cell.

The relative amounts of the different species were evaluated from the variations of the subspectrum areas and the recoil-free fractions. They are found to vary linearly with the number of inserted lithium ions in line with the reaction given by Eq. (1.10). The value of the saturation magnetization of the fully lithiated electrode material at 4 K is close to that of bulk α-Fe. The zero-field cooling and field cooling curves obtained at different stages of discharge show the progressive formation of super-paramagnetic α-Fe nanoparticles with a constant average diameter of about 3 nm. This result is consistent with the extrusion of Fe atoms from $FeSn_2$ during the conversion reaction and the formation of α-Fe nanoparticles.

For nanostructured $FeSn_2$, the voltage profile is a smooth curve decreasing as lithiation proceeds, instead of the plateau observed for the $FeSn_2$ microparticles (Figure 1.11). However, the observed changes in ^{57}Fe and ^{119}Sn Mössbauer spectra are also consistent with the conversion reaction given by Eq. (1.10) [44]. This indicates that nanostructured and crystalline $FeSn_2$ are both transformed into a Li_7Sn_2/α-Fe nanocomposite during the first discharge. Thus, the first discharge should be considered as a restructuring step for the electrode material, while α-Fe/Li_7Sn_2 nanocomposite is the real starting material for the reversible cycles.

During the first charge of $FeSn_2$ microparticles, the operando ^{119}Sn Mössbauer spectra change from the asymmetrical peak of Li_7Sn_2 into a broad doublet and the average isomer shift increases linearly from 1.8 to 2.3 mm·s^{-1}. According to Eq. (1.8), this corresponds to changes in chemical composition from Li_7Sn_2 to LiSn. The observed reverse trend for the second discharge is consistent with the reversibility of the mechanism but strongly differs from the first discharge. The ^{57}Fe Mössbauer spectra do not change significantly during this first charge and the second discharge, showing that the α-Fe nanoparticles do not react with Sn during the reversible cycles. Thus, the reversible mechanism of $FeSn_2$ based electrodes consists of Li_xSn alloying–dealloying reactions. The α-Fe nanoparticles and carbon additives form a composite matrix that buffers the volume variations of Li_xSn during cycling and improves the electronic conductivity of the electrode.

MSn$_x$ Intermetallic Compounds (M = Mn, Co, Ni, Cu) Other tin-based intermetallics have been considered as anode materials for Li-ion batteries. This includes MnSn$_2$ [45, 46], CoSn$_2$ [47, 48], Ni$_3$Sn$_4$ [49–51], and Cu$_6$Sn$_5$ [52–54]. The voltage profiles of the first three compounds are similar to that of FeSn$_2$ (see Figure 1.11) except for the voltage value of the first discharge plateau and the existence of an additional plateau during the charge for MnSn$_2$. The voltage profile of Cu$_6$Sn$_5$ is more complex, involving intermediate Li–Cu–Sn phases, and is not discussed here. In the same way as FeSn$_2$, the ^{119}Sn Mössbauer spectra obtained during the first discharge of MnSn$_2$, CoSn$_2$, and Ni$_3$Sn$_4$ show the direct transformation of the pristine material into M/Li$_7$Sn$_2$ (M = Mn, Co, Ni) nanocomposites. The situation is more complex for the first charge. The average isomer shift increases as delithiation proceeds for CoSn$_2$ [47] and nanostructured MnSn$_2$ [46] but the spectra are broadened, reflecting the formation of Li–Co–Sn and Li–Mn–Sn ternary phases, respectively, or strong chemical bonds between Li$_x$Sn and metallic nanoparticles. In addition, the voltage curve of MnSn$_2$ shows an additional plateau at the end of charge. The ^{119}Sn Mössbauer spectra obtained at this voltage reflect magnetic relaxation. This was explained by the existence of magnetic MnSn$_2$ particles within the electrode, resulting from partial back reaction of Sn-rich Li$_x$Sn with Mn. For Ni$_3$Sn$_4$, the Mössbauer spectrum obtained at the end of the first charge is close to that of the pristine material and can be attributed to the reaction of Sn atoms with Ni nanoparticles [49].

Thus, depending on the transition metal M (Mn, Fe, Co, Ni), back reactions of Sn with M atoms take place at different levels during the delithiation process. Such back reactions that prevent Sn coalescence could improve the cycle life. Although the first and second discharges differ, they both end with the formation of a M/Li$_7$Sn$_2$ nanocomposite. The nanostructuration of the first discharge is irreversible, while the cycle formed by the first charge and the second discharge is typical of the reversible cycles. They reflect Li–Sn alloying reactions with possible back reactions between M and Sn atoms. The M/C matrix formed during the first discharge improves the cycle life compared to β-Sn. However, the capacity remains too low for the next generation of high energy Li-ion batteries, and addition of Si was proposed to improve the electrochemical performance.

MSn$_x$/Si Composites Si can electrochemically react with up to 3.75 Li at room temperature, leading to a theoretical capacity of 3580 mAh·g^{-1}, which is about four times higher than that of β-Sn. The electrochemical mechanism of crystalline Si with Li differs from that of β-Sn and is based on Li$_x$Si alloying–dealloying reactions with the formation of amorphous phases, but still at a low voltage [55]. Thus, the addition of silicon to tin intermetallics is expected to significantly increase the capacity of the negative electrode materials for Li-ion batteries. Better performance was indeed obtained for the Ni$_3$Sn$_4$/Si/C composite that shows higher specific capacity than Ni$_3$Sn$_4$ [56]. Both Ni$_3$Sn$_4$ and Si are electrochemically active in the composite and the operando ^{119}Sn Mössbauer spectra obtained during the charge/discharge cycles are similar to those found for Ni$_3$Sn$_4$ negative electrode material. They show the formation of a Ni/Li$_7$Sn$_2$ nanocomposite during the first discharge, followed by reversible cycles of Li$_x$Sn alloying–dealloying reactions

including the back reaction of Ni with Sn atoms during the charge processes. Both Li_xSi and Li_xSn alloying reactions go along with strong volume variations, but the Ni/C matrix maintains the electronic conductivity and the dispersion of the electrochemically active particles, while the gradual formation of porosity in the electrode film upon cycling helps to buffer the volume variations and the electrolyte impregnation. As a result, a capacity of $800\,mA.g^{-1}$ over 200 cycles was obtained with a capacity loss at first cycle lower than 20%. Other Si-enriched Sn-intermetallic based composites have been proposed, showing improved performance [57–59].

1.2.3 Iron-Based Electrode Materials

1.2.3.1 LiFePO$_4$ as Positive Electrode Material for Li-ion Batteries

Lithium metal oxides with layered structure are commonly used as positive electrode materials for Li-ion batteries. The lithium ions are intercalated between the layers, leading to rather high specific capacity and operating voltage. However, there are some issues regarding the cycle life, rate capability, and safety due to the layered structure. $LiFePO_4$ with olivine structure is an interesting positive electrode material that overcomes these limitations, but has a lower energy density [60]. The voltage curves obtained for $LiFePO_4$ in a Li half-cell and galvanostatic regime are formed by similar plateaus for charge and discharge at $3.4\,V$ that are typical of reversible two-phase reactions. At room temperature, the ^{57}Fe Mössbauer spectrum of $LiFePO_4$ is a doublet ($\delta = 1.22\,mm \cdot s^{-1}$, $\Delta = 2.96\,mm \cdot s^{-1}$), reflecting high spin Fe^{2+}. The intensity of this doublet decreases during delithiation (charge) while the intensity of another doublet ($\delta = 0.45\,mm \cdot s^{-1}$, $\Delta = 1.52\,mm \cdot s^{-1}$) increases. The latter doublet is typical of high spin Fe^{3+} in $FePO_4$ [61]. The $LiFePO_4$–$FePO_4$ two-phase reaction is found to be reversible for the lithiation (discharge) and the relative amounts of $LiFePO_4$ and $FePO_4$, evaluated from the relative contributions of the Fe^{2+} and Fe^{3+} subspectra, vary linearly with the number of inserted lithium ions [62, 63].

The substitution of Mn (or Co) for Fe in $LiFePO_4$ has been proposed to increase the electrode potential and, as a result, the energy density of the battery. The partial substitution of Mn for Fe leads to a voltage profile with two plateaus at 3.4 and $4\,V$ instead of only one plateau at $3.4\,V$ for $LiFePO_4$ [64]. The operando ^{57}Fe Mössbauer spectra (Figure 1.13) and the XRD patterns were measured for the first cycle of $Li_xMn_{0.25}Fe_{0.75}PO_4$ in Li half-cell.

For $0.55 < x < 0.95$, the Mössbauer spectra show the progressive oxidation of Fe(II) ($\delta = 1.3\,mm \cdot s^{-1}$, $\Delta = 3.0\,mm \cdot s^{-1}$) into Fe(III) ($\delta = 0.42\,mm \cdot s^{-1}$, $\Delta = 1.10\,mm \cdot s^{-1}$) with a quadrupole splitting lower than that of $FePO_4$, and another doublet attributed to Fe(II) ($\delta = 1.23\,mm \cdot s^{-1}$, $\Delta = 2.75\,mm \cdot s^{-1}$), suggesting the existence of a new iron-based phase. The intensity of the Bragg peaks of $LiMn(II)_{0.25}Fe(II)_{0.75}PO_4$ obtained by operando XRD [64] decreases as charge proceeds, while the intensity increases for the new phase, attributed to $Li_{0.55}Fe(II)_{0.3}Fe(III)_{0.45}Mn(II)_{0.25}PO_4$. For $0.25 < x < 0.55$, there is a sloppy voltage increase up to $4.0\,V$ and a systematic shift of the (020) diffraction peak of $Li_{0.55}Fe(II)_{0.3}Fe(III)_{0.45}Mn(II)_{0.25}PO_4$. This indicates that the reaction with lithium is monophasic, ending with $Li_{0.25}Fe(III)_{0.75}Mn(II)_{0.25}PO_4$. The Fe(II) isomer shift and quadrupole splitting

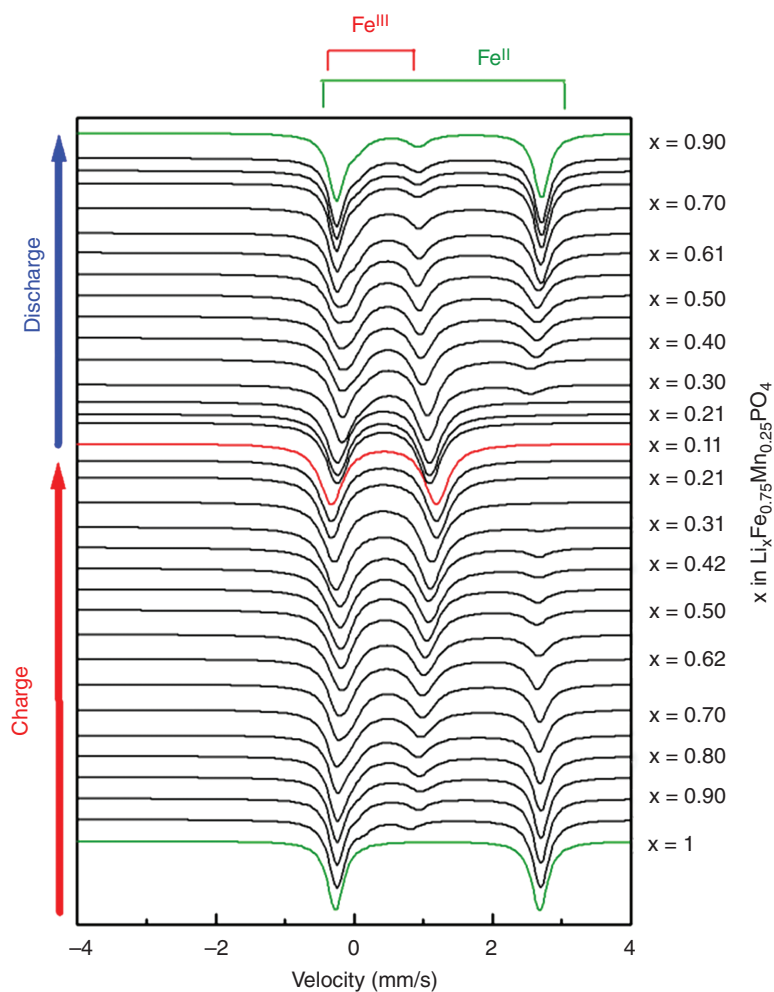**Figure 1.13** ^{57}Fe Mössbauer spectra collected during the first galvanostatic charge–discharge cycle of LiMn$_{0.25}$Fe$_{0.75}$PO$_4$ in Li half-cell. Source: Reproduced from Ref. [64]/with permission from Springer Nature.

and the Fe(III) isomer shift remain unchanged while the quadrupole splitting of Fe(III) increases gradually. This was attributed to the increasing disorder around Fe(III). For $0.1 < x < 0.25$, corresponding to the voltage plateau at 4 V, Mn(II) is oxidized into Mn(III). The Mössbauer spectra were fitted to the doublet of Li$_{0.25}$Fe(III)$_{0.75}$Mn(II)$_{0.25}$PO$_4$ and an additional Fe(III) doublet ($\delta = 0.42$ mm·s^{-1}, $\Delta = 1.50$ mm·s^{-1}) attributed to Fe(III)$_{0.75}$Mn(III)$_{0.25}$PO$_4$.

1.2.3.2 Fe$_{1.19}$PO$_4$(OH)$_{0.57}$(H$_2$O)$_{0.43}$/C as Positive Electrode Material for Li-ion Batteries

Fe$_{1.19}$PO$_4$(OH)$_{0.57}$(H$_2$O)$_{0.43}$/Cnt (FPHH/Cnt, Cnt: carbon nanotubes) has been proposed as a positive electrode material for Li-ion batteries [65]. This composite, obtained by hydrothermal synthesis, has a specific capacity of 120 mAh·g^{-1} at 1 C for
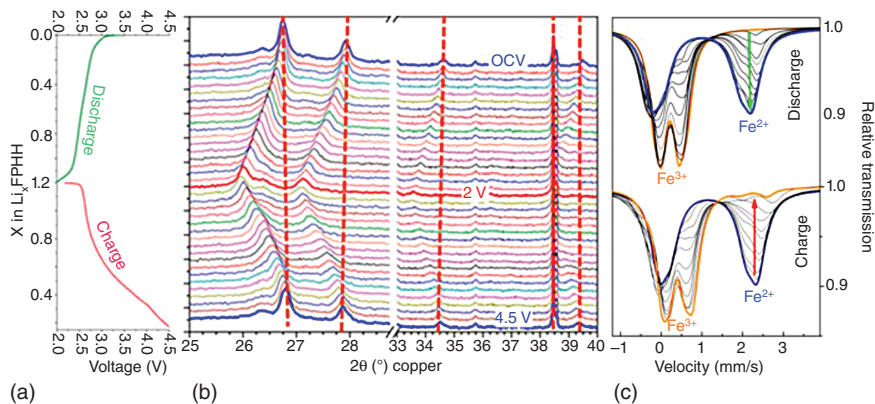
Figure 1.14 First cycle of FPHH based electrode material in Li half-cell: voltage curves (a), operando XRD patterns in the range $2\theta = 25–28.5°$ and $33–40°$ (b), operando ^{57}Fe Mössbauer spectra (c). Source: Reproduced from Ref. [65]/with permission from American Chemical Society.

500 cycles and shows unusual lithium insertion mechanism. The structure of FPHH ($I4_1/amd$) can be described by perpendicular chains of face sharing iron octahedra along 100 and 010 directions and connected by PO_4 tetrahedra. There is one crystallographic site for Fe with 59% occupation, but the existence of Fe vacancies and O—H bonds are responsible for Fe position disorder. The ^{57}Fe Mössbauer spectrum of FPHH was fitted to two doublets with the same isomer shift: $\delta = 0.4$ mm·s^{-1} (high spin Fe^{3+}) but different quadrupole splittings: $\Delta = 0.33$ mm·s^{-1} and 0.67 mm·s^{-1}, reflecting the distribution of Fe—O bonds and Fe vacancies. The Li$^+$ diffusion paths are along 100 and 010 channels interconnected by Fe vacancies.

The voltage profile of the first cycle is typical of a one-phase reaction (Figure 1.14). This is confirmed by operando XRD that shows continuous variations in the position of the Bragg peaks of FPHH, in line with the increase and the decrease of the cell volume (~10%) during the discharge and charge, respectively. The Mössbauer spectra change as lithiation proceeds from one doublet for FPHH with an average isomer shift, $\delta_{av} = 0.4$ mm·s^{-1}, typical of Fe^{3+}, to a spectrum formed by two asymmetrical peaks with the average Mössbauer parameters: $\delta_{av} = 1.04$ mm·s^{-1}, $\Delta_{av} = 2.2–2.6$ mm·s^{-1}, typical of high spin Fe^{2+}. The shape and the linewidth of the Mössbauer peaks reflect quadrupole splitting distributions. The evolution of these distributions during the charge–discharge cycle is due to changes in the local environment of Fe atoms. This evolution and the variations of the lattice parameters with Li content reflect a more complex mechanism than a random occupation of the vacant sites by Li. A mechanism based on the selective occupation of iron and channel vacancies that affects both Fe^{2+} and Fe^{3+} environments has been proposed [65].

1.2.3.3 $Na_{1.5}Fe_{0.5}Ti_{1.5}(PO_4)_3$/C as Electrode Material for Na-ion Batteries

Phosphate compounds with Nasicon structure (sodium super ionic conductor) form an attractive family of electrode materials for Na-ion batteries due to the flexibility of the structure and the existence of a lot of vacant sites for Na$^+$ insertion. Carbon coated $Na_{1.5}Fe_{0.5}Ti_{1.5}(PO_4)_3$/C can be used as negative or positive electrode material

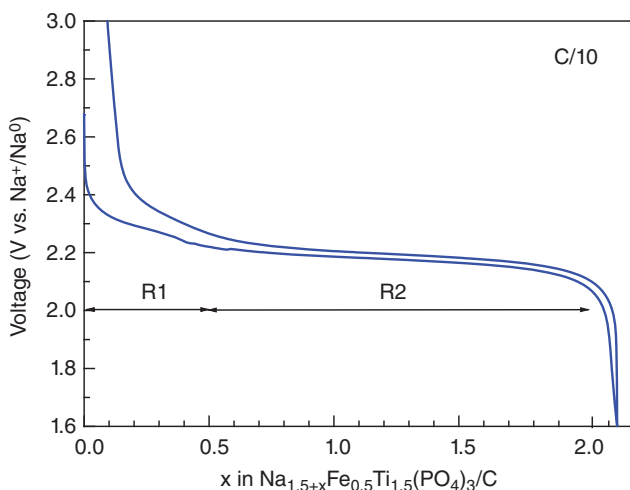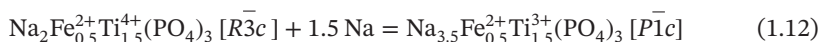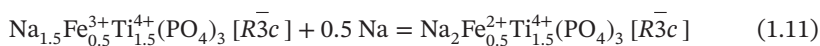**Figure 1.15** Voltage curve of the first cycle of $Na_{1.5}Fe_{0.5}Ti_{1.5}(PO_4)_3/C$ in Na half-cell and galvanostatic regime (0.1 Na per hour). Two different mechanisms are observed in regions R1 and R2. Source: Reproduced from Ref. [66]/with permission from American Chemical Society.

for Na-ion batteries due to the existence of two voltage plateaus. $Na_{1.5}Fe_{0.5}Ti_{1.5}(PO_4)_3$ has a rhombohedral structure (R-3c) with a random occupation of the metal sites by Fe and Ti. The ^{57}Fe Mössbauer spectrum is formed by a doublet due to high spin Fe^{3+} while that of $Na_{1.5}Fe_{0.5}Ti_{1.5}(PO_4)_3/C$ shows an additional doublet due to high spin Fe^{2+} in impurities arising from pyrolysis (9 at%) [66, 67].

The voltage curve of the first cycle of $Na_{1.5}Fe_{0.5}Ti_{1.5}(PO_4)_3/C$ in a Na half-cell is shown in Figure 1.15. During the first discharge, the voltage decreases from 2.4 to 2.2 V in the range 0–0.5 Na per f.u. (formula unit), suggesting a one-phase reaction (Region R1), and then forms a plateau until the end of sodiation at 2.1 Na per f.u. (Region R2), reflecting a two-phase reaction. This two-step mechanism is reversible for the first charge. The plateau at 2.2 V is also observed for $NaTi_2(PO_4)_3$ and can be attribute to the redox couple Ti^{4+}/Ti^{3+} [68].

The operando ^{57}Fe Mössbauer spectra obtained during the first discharge show the reduction of high spin Fe^{3+} into high spin Fe^{2+} ($\delta = 1.2\,mm\cdot s^{-1}$, $\Delta = 2.7\,mm\cdot s^{-1}$) in region R1. Then, the spectra do not change anymore in region R2 (Figure 1.16).

Deeper insight in the mechanism was obtained by operando XRD [66], confirming that the first discharge is a solid solution reaction coming with the reduction of Fe^{3+} into Fe^{2+}, followed by a two-phase reaction, leading to the reduction of Ti^{4+} into Ti^{3+}:

$$Na_{1.5}Fe^{3+}_{0.5}Ti^{4+}_{1.5}(PO_4)_3\ [R\bar{3}c\,] + 0.5\,Na = Na_2Fe^{2+}_{0.5}Ti^{4+}_{1.5}(PO_4)_3\ [R\bar{3}c\,] \quad (1.11)$$

$$Na_2Fe^{2+}_{0.5}Ti^{4+}_{1.5}(PO_4)_3\ [R\bar{3}c\,] + 1.5\,Na = Na_{3.5}Fe^{2+}_{0.5}Ti^{3+}_{1.5}(PO_4)_3\ [P\bar{1}c] \quad (1.12)$$

These two reactions are reversible for the first charge and form the basic mechanism for the charge–discharge cycles. The observed better cyclability and
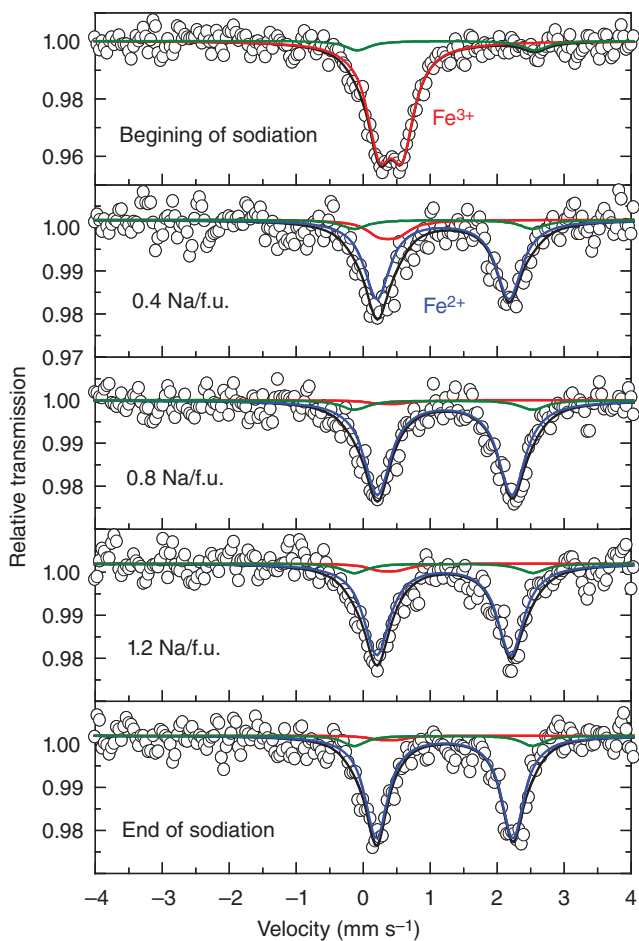
Figure 1.16 Operando ^{57}Fe Mössbauer spectra obtained for the first discharge (sodiation) of $Na_{1.5}Fe_{0.5}Ti_{1.5}(PO_4)_3$/C in Na half-cell. Source: Reproduced from Ref. [66]/with permission from American Chemical Society.

rate capability of $Na_{1.5}Fe_{0.5}Ti_{1.5}(PO_4)_3$/C compared to $NaTi_2(PO_4)_3$/C have been attributed to improved Na^+ diffusion resulting from the solid solution mechanism in R1.

1.3 Mössbauer Spectroscopy of Tin-Based Catalysts

1.3.1 Reforming Catalysis

Alumina-supported bimetallic Pt-Sn catalysts have been proposed to accelerate dehydrogenation, isomerization, and dehydrocyclization reactions in order to increase the gasoline octane number. Addition of tin to monometallic Pt/Al_2O_3
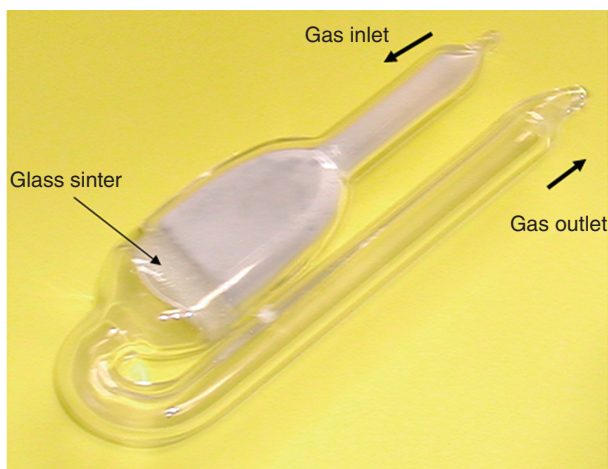
Figure 1.17 Specific cell for in situ ^{119}Sn Mössbauer measurements of Sn-based catalysts.

improves the selectivity and stability of reforming catalysts by reducing their deactivation caused by coke formation (reaction step) and the coalescence of metallic particles (regeneration step). The redox reactions with Pt-Sn/Al$_2$O$_3$ were studied by ^{119}Sn Mössbauer spectroscopy in order to evaluate the effects of the synthesis method, the sample composition, and the experimental conditions of reduction/oxidation on the nature and reactivity of tin species. In situ measurements were performed to follow the evolution of the catalyst during the oxidation/reduction cycles with a lab-made cell (Figure 1.17).

1.3.2 Redox Properties of Pt-Sn Based Catalysts

A Mössbauer δ–Δ correlation diagram has been established from the characterization of Sn/Al$_2$O$_3$ and Pt-Sn/Al$_2$O$_3$ samples (Figure 1.18) [69]. The tin oxidation states
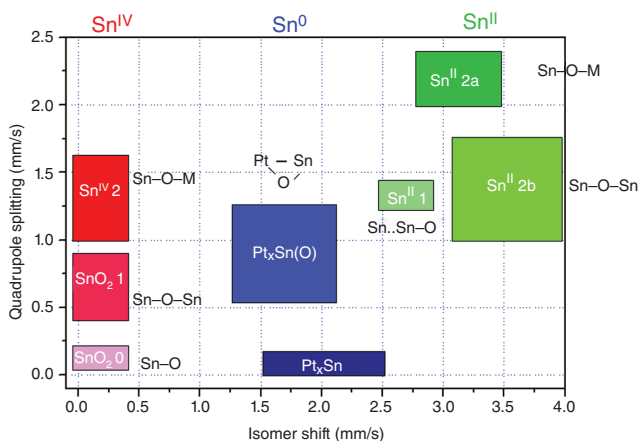

Figure 1.18 Correlation diagram for Sn species in Pt$_x$Sn phases and Sn-based catalysts. Source: Reproduced from Ref. [69]/with permission from Springer Nature.

Sn(IV), Sn(II), and Sn(0) were identified from the values of the isomer shift, while the values of the quadrupole splitting have allowed to distinguish different Sn local environments. This includes three types of Sn(IV): "SnO$_2$ 0" in SnO$_6$ free units, "SnO$_2$ 1" in SnO$_2$-like lattices, and "Sn(IV) 2" in Sn(IV)–O–M bridges with M = Al, Pt; two types of Sn(0): "Pt$_x$Sn" and "Pt$_x$Sn(O)" close to oxygen; and three types of Sn(II): "Sn(II) 1" in SnO-like structure, "S(II) 2a" in Sn(II)–O–M bridges, and "Sn(II) 2b" in Sn(II)–O–Sn(II) bridges.

The correlation diagram was used to explain the phase transformations occurring in the Pt-Sn particles of Pt-Sn/Al$_2$O$_3$ samples prepared by sol-gel or impregnation methods, after oxidation and reduction [70]. The reaction mechanisms between Sn–(n–C$_4$H$_9$)$_4$ and alumina surface sites were also identified in order to optimize the controlled preparation of Pt-Sn/Al$_2$O$_3$ catalysts [71]. A structural model was given that describes the morphology of the bimetallic particles and their evolution under
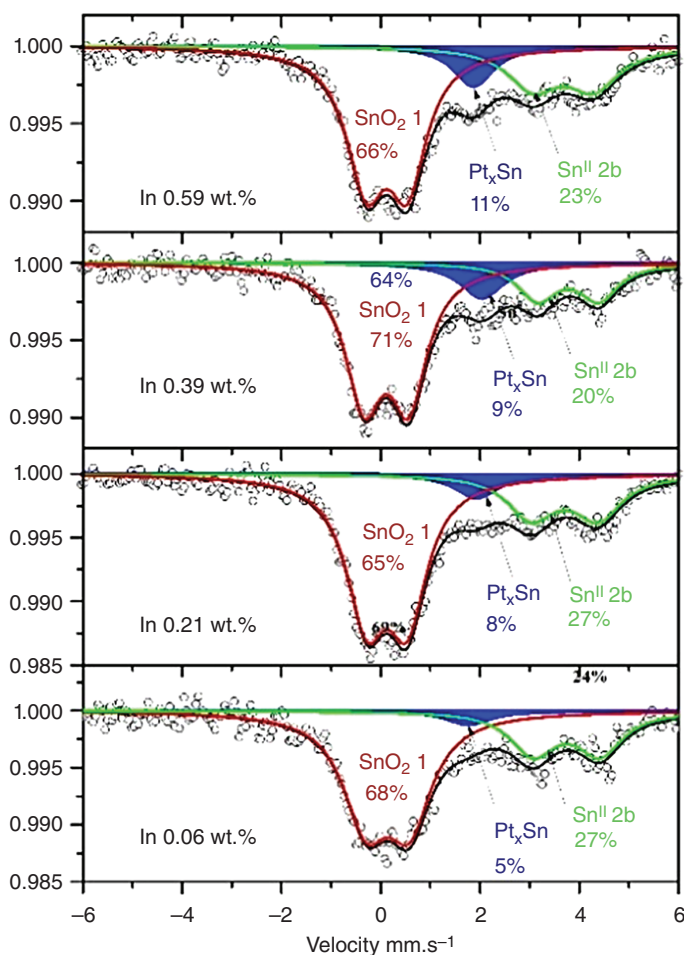

Figure 1.19 ^{119}Sn Mössbauer spectra of reduced catalysts Pt-Sn-In/Al$_2$O$_3$ –Cl (CP) with different indium loadings. Source: Reproduced from Ref. [69]/with permission from Springer Nature.

various heat treatments at the atomic scale. This model was used to optimize the preparation method of Pt-Sn/Al$_2$O$_3$ catalysts in order to preferentially anchor Pt next to Sn particles and improve the catalytic activity. The results are very promising for applications [72, 73].

1.3.3 Trimetallic Pt-Sn-In Based Catalysts

Trimetallic naphtha-reforming catalysts comprising Pt-Sn modified by the addition of indium (Pt/Al$_2$O$_3$SnIn–Cl) show high selectivity due to the addition of In as second promoter [14]. Different samples synthesized by coprecipitation (CP), successive impregnations (SI), and surface organostannic chemistry of metals (SOMC) were investigated by ^{119}Sn Mössbauer spectroscopy. The correlation diagram of Figure 1.18 was used to identify various Sn-based species. The presence of In in Pt/Al$_2$O$_3$SnIn–Cl obtained by CP of Sn and In with alumina precursor, followed by sol-gel method, favors the formation of Pt$_x$Sn alloys [74]. Figure 1.19 shows the Mössbauer spectra of different Pt/Al$_2$O$_3$SnIn$_y$–Cl samples reduced at 500 °C under H$_2$. The formation of Pt$_x$Sn alloys during the reduction step is observed for all the samples and the increase of isomer shift with increasing indium content y indicates
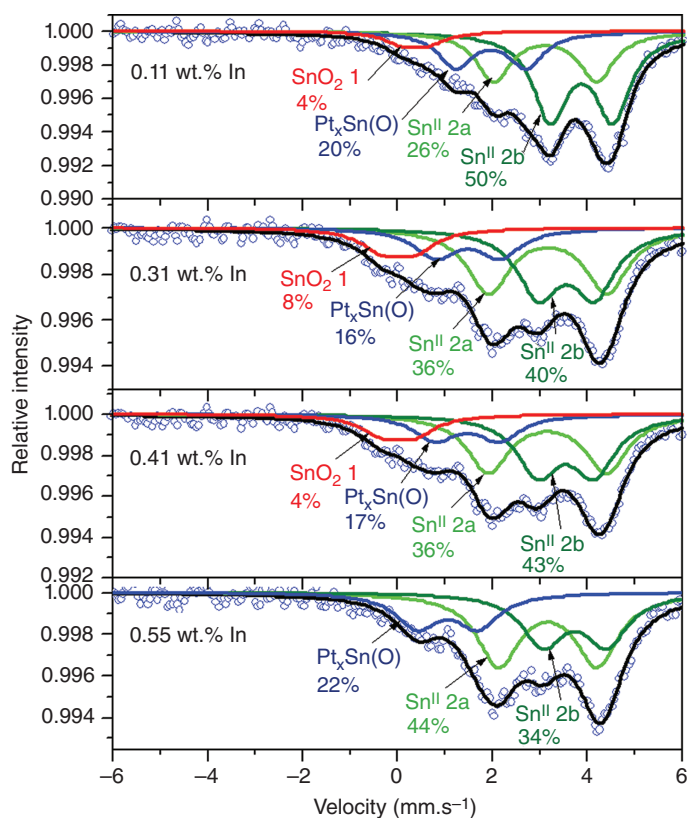

Figure 1.20 ^{119}Sn Mössbauer spectra of reduced catalysts Pt-Sn-In/Al$_2$O$_3$ –Cl (SI) with different indium loadings.

changes in the chemical composition of Pt_xSn from Pt_3Sn to $PtSn$. As y increases, more Sn oxides are in a weak interaction with alumina, and Pt-Sn alloying becomes possible with higher tin atomic concentration in the formed alloys.

The presence of indium in $Pt-Sn-In/Al_2O_3$–Cl catalysts, obtained by SI of metals, leads to the formation of $Pt_xSn(O)$ oxo-metallic phases [75]. The Mössbauer spectrum obtained for 0.11 wt% of In can be fitted to four subspectra that can be assigned to unreduced "Sn(IV) 1" oxide, "Sn(II) 2a" and "Sn(II) 2b" oxides, and oxo-metallic $Pt_xSn(O)$ phase (Figure 1.20). The other spectra obtained for 0.31, 0.41, and 0.55 wt% of In also show oxo-metallic phases that represent 16, 17, and 22% of the Sn species, respectively. The isomer shift of $Pt_xSn(O)$ decreases with increasing In content, which indicates that x increases. Such a decrease in the Sn atomic concentration agrees with the substitution of Sn by In and proves the close Pt–In proximity in these catalysts.

Improving the formation of Pt_xSn alloyed clusters on γ-alumina with a high Sn(0)/Pt ratio represents a crucial step toward more selective heterogeneous

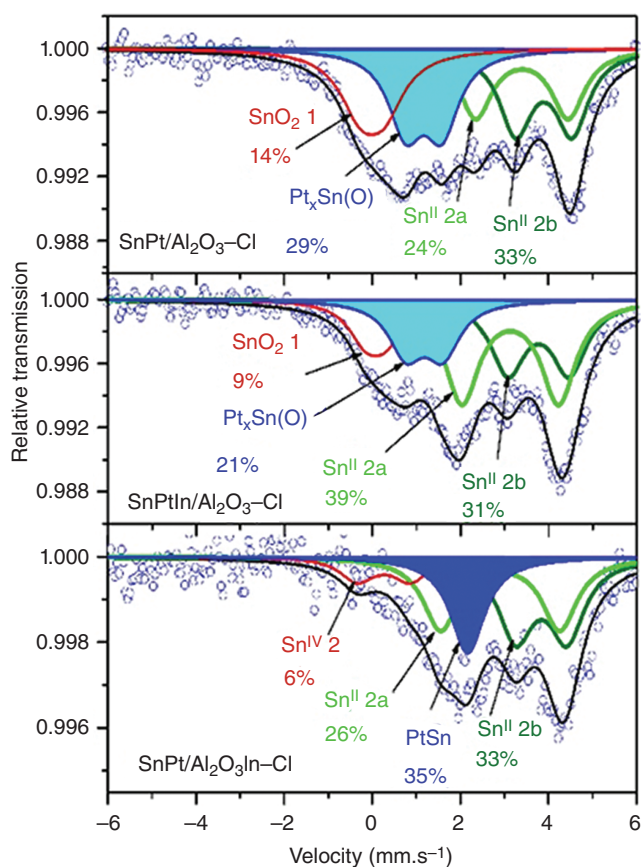**Figure 1.21** ^{119}Sn Mössbauer spectra of reduced catalysts obtained by SOMC: Sn-Pt/Al_2O_3–Cl, Sn-Pt-In/Al_2O_3–Cl (In by SI), and Sn-Pt/Al_2O_3In–Cl (In by CP). Source: Reproduced from Ref. [76]/with permission from American Chemical Society.

catalysts [76]. For that purpose, bimetallic Sn-Pt and trimetallic Sn-Pt-In-based catalysts were prepared by SOMC on monometallic Pt and bimetallic Pt-In-based catalysts, respectively. The ^{119}Sn Mössbauer spectra of reduced Sn-Pt/Al$_2$O$_3$–Cl, Sn-Pt-In/Al$_2$O$_3$–Cl (In added by impregnation), and Sn-Pt/Al$_2$O$_3$In–Cl (In added by CP with alumina source) are shown in Figure 1.21. The spectra of Sn-Pt/Al$_2$O$_3$–Cl and Sn-Pt-In/Al$_2$O$_3$–Cl show the contribution of Pt$_x$Sn(O) species but not of Pt$_x$Sn alloys, in contrast to Sn-Pt/Al$_2$O$_3$In–Cl. Pt-Sn alloying is favored in the latter case, when In is introduced in the support via CP. This can be explained by the existence of In(III) species to stabilize Pt$_x$Sn at the interface with the alumina support.

The application of ^{119}Sn Mössbauer spectroscopy to ternary Pt-Sn-In based systems provides some explanations about the effect of indium as a function of its introduction method, its loading, and the introduction method of the other elements (Pt, Sn). The CP catalysts have higher Sn(0)/Pt ratios than SI catalysts where the elements were initially thought to be closer to Pt due to the preparation method. This is attributed to the presence of Pt$_x$Sn alloys in CP catalysts only and to the substitution of Sn in Pt$_x$Sn(O) by surface indium in SI catalysts. The observed differences in the activity and selectivity of the two differently prepared Pt-Sn-In systems can be related to the Sn(0)/Pt ratio [77].

1.4 Conclusion

In this chapter, we have presented different applications of ^{57}Fe and ^{119}Sn Mössbauer spectroscopies to energy materials, including electrode materials for Li-ion and Na-ion batteries and tin-based catalysts.

The Mössbauer spectroscopy can be used for the characterization of pristine electrode materials but also as an operando technique to follow electrochemical reactions. The examples considered here have been selected to illustrate the three main types of reactions encountered in electrode materials for batteries. The first one is referred to as an alloying reaction where x Li atoms react with a p-block atom M to reversibly form Li$_x$M. About 4 Li can react with Sn ($x \approx 4$), which explains the high specific capacity of Sn-based electrode materials although they contain a heavy element. However, alloying reactions are associated with strong volume variations that limit the cycle life of batteries. Tin intermetallics have been proposed to overcome this problem. In that case, the first lithiation is a conversion reaction that transforms the pristine material into a nanocomposite for cycling. This is the second type of reaction that also occurs for tin oxides and composites. For both alloying and conversion reactions, the Mössbauer spectroscopy has been mainly used to identify the electrochemically formed species that are often nanosized and poorly crystallized. Finally, the insertion reactions involve Li$^+$ diffusion on the vacant sites of a host material as often encountered in positive electrode materials containing transition metals. Such reactions go along with the reduction and oxidation of metal ions due to lithiation and delithiation, respectively. In the case of iron-based electrode materials, the ^{57}Fe Mössbauer spectroscopy has been mainly used to detect changes in the oxidation state of Fe or of other metal elements in its environment.

Some examples of supported alumina bimetallic Pt-Sn and trimetallic Pt-Sn-In catalysts have been discussed. In that case, in situ Mössbauer spectroscopy has been used for the identification of tin species formed during the oxidation and reduction steps. The proposed approach, based on the use of an isomer shift – quadrupole splitting correlation diagram, has allowed to identify the most interesting tin species with improved performance and to optimize the synthesis methods.

Mössbauer spectroscopy provides reliable information on complex reaction mechanisms observed in electrochemistry and catalysis. However, an accurate analysis of such mechanisms often requires to combine different in situ measurements, as shown in this chapter for XRD and Mössbauer spectroscopy. Undoubtedly, the use of synchrotron radiation could also be of great interest to expand the field of applications to other elements apart from Fe and Sn and to reduce the measurement time.

Acknowledgments

References

1 Goodenough, J.B., Whittingham, M.S., and Yoshino, A. (2019). The Nobel Prize in Chemistry 2019. NobelPrize.org. Nobel Prize Outreach AB 2023. www .nobelprize.org/prizes/chemistry/2019/summary. (accessed 4 February 2023).

2 Larcher, D. and Tarascon, J.M. (2015). Towards greener and more sustainable batteries for electrical energy storage. *Nat. Chem.* 7 (1): 19–29.

3 Obrovac, M.N. and Chevrier, V.L. (2014). Alloy negative electrodes for Li-ion batteries. *Chem. Rev.* 114 (23): 11444–11502.

4 Besenhard, J.O., Yang, J., and Winter, M. (1997). Will advanced lithium-alloy anodes have a chance in lithium-ion batteries? *J. Power Sources* 68 (1): 87–90.

5 Larcher, D., Beattie, S., Morcrette, M. et al. (2007). Recent findings and prospects in the field of pure metal as negative electrodes for Li-ion batteries. *J. Mater. Chem.* 17 (36): 3759–3772.

6 Winter, M. and Besenhard, J.O. (1999). Electrochemical lithiation of tin and tin based intermetallics and composites. *Electrochim. Acta* 45 (1–2): 31–50.

7 Zhang, W.J. (2011). Structure and performance of $LiFePO_4$ cathode materials: a review. *J. Power Sources* 196 (6): 2962–2970.

8 Barpanda, P., Ati, M., Melot, B.C. et al. (2011). A 3.90 V iron-based fluorosulphate material for lithium-ion batteries crystallizing in the triplite structure. *Nat. Mater.* 10 (10): 772–779.

9 Palomares, V., Serra, P., Villaluenga, I. et al. (2012). Na-ion batteries, recent advances and present challenges to become low cost energy storage systems. *Energy Environ. Sci.* 5 (3): 5884–5901.

10 Hu, Y.S., Komaba, S., Forsyth, M. et al. (2019). A new emerging technology: Na-ion batteries. *Small Methods* 3 (4): 1900184.

11 Tarascon, J.M. (2010). The greatness of Mössbauer spectroscopy to the design of better Li-ion batteries. *Möss. Eff. Ref. Data J.* 33 (2): 53–54.

12 Lippens, P.E., El Khalifi, M., Chamas, M. et al. (2012). How Mössbauer spectroscopy can improve Li-ion batteries. *Hyperfine Interact.* 206 (1–3): 35–46.

13 Dautzenberg, F.M., Helle, J.N., Biloen, P., and Sachtler, H. (1980). Conversion of n-hexane over mono-functional supported and unsupported PtSn catalysts. *J. Catal.* 63 (1): 119–128.

14 Le Goff, P.Y., Le Peltier, F., Giraud, J. et al. (2010). Bimetallic or multi-metallic catalyst that has an optimized bimetallicity index and an optimized hydrogen adsorption capacity. Fr Patent 2910347, filed 7 December 2007 and issues 25 February 2010.

15 Berry, F. (1984). *Mössbauer Spectroscopy Applied to Inorganic Chemistry* (ed. G.J. Long), 391–442. New York and London: Plenum Press.

16 Li, X., Zhu, K., Pang, J. et al. (2018). Unique role of Mössbauer spectroscopy in assessing structural features of heterogeneous catalysts. *Appl. Catal. B Environ.* 224: 518–532.

17 Harks, P.P.R.M.L., Mulder, F.M., and Notten, P.H.L. (2015). In situ methods for Li-ion battery research: a review of recent developments. *J. Power Sources* 288 (1): 92–105.

18 Jumas, J.C., Fullenwarth, J., Sougrati, M.T. et al. (2014). Analysis of the features of an electrode material of an electrochemical cell. WO Patent 2014033402-A1, filed 28 August 2013 and issued 6 March 2014.

19 Lippens, P.E. and Jumas, J.C. (2010). It's all about the battery. *Möss. Eff. Ref. Data J.* 33 (2): 31–54.

20 Leriche, J.B., Hamelet, S., Shu, J. et al. (2010). An electrochemical cell for operando study of lithium batteries using synchrotron radiation. *J. Electrochem. Soc.* 157 (5): A606–A610.

21 Sivasankaran, V., Marino, C., Chamas, M. et al. (2011). Improvement of intermetallics electrochemical behavior by playing with the composite electrode formulation. *J. Mater. Chem.* 21 (13): 5076–5082.

22 Courtney, I.A., Tse, J.S., Mao, O. et al. (1998). *Ab initio* calculation of the lithium-tin voltage profile. *Phys. Rev. B* 58 (23): 15583–15588.

23 Lippens, P.E., Aldon, L., Ionica, C.M. et al. (2005). Characterization of Li insertion mechanisms in negative electrode materials for Li-ion batteries by Mössbauer spectroscopy and first-principles calculations. In: *Solid State Ionics-2004*, vol. 842 (ed. P. Knauth, C. Masquelier, E. Traversa, et al.), 249–260. Warrendale.

24 Sangster, J. and Bale, C.W. (1998). The Li-Sn (lithium-tin) system. *J. Phase Equilib.* 19 (1): 70–75.

25 Dunlap, R.A., Small, D.A., MacNeil, D.D. et al. (1999). A Mössbauer effect investigation of the Li–Sn system. *J. Alloys Compd.* 289 (1–2): 135–142.

26 Robert, F., Lippens, P.E., Olivier-Fourcade, J. et al. (2007). Mössbauer spectra as a fingerprint in tin-lithium compounds: applications to Li-ion batteries. *J. Solid State Chem.* 180 (1): 339–348.

27 Naille, S., Jumas, J.C., Lippens, P.E. et al. (2009). ^{119}Sn Mössbauer parameters as predictive tool for future Sn-based negative electrode materials. *J. Power Sources* 189 (1): 814–817.

28 Chouvin, J., Olivier-Fourcade, J., Jumas, J.C. et al. (1999). ^{119}Sn Mössbauer study of Li$_x$Sn alloys prepared electrochemically. *Chem. Phys. Lett.* 308 (5–6): 413–420.

29 Idota, Y., Kubota, T., Matsufuji, A. et al. (1997). Tin-based amorphous oxide: a high-capacity lithium-ion-storage material. *Science* 276 (5317): 1395–1397.

30 Sandu, I., Brousse, T., Schleich, D.M. et al. (2004). SnO$_2$ negative electrode for lithium ion cell: *in situ* Mössbauer investigation of chemical changes upon discharge. *J. Solid State Chem.* 177 (11): 4332–4340.

31 Chouvin, J., Olivier-Fourcade, J., Jumas, J.C. et al. (2000). SnO reduction in lithium cells: study by X-ray absorption, ^{119}Sn Mössbauer spectroscopy and X-ray diffraction. *J. Electroanal. Chem.* 494 (2): 136–146.

32 Courtney, I.A., Dunlap, R.A., and Dahn, J.R. (1999). *In-situ* 119Sn Mössbauer effect studies of the reaction of lithium with SnO and SnO: 0.25 B$_2$O$_3$: 0.25 P$_2$O$_5$ glass. *Electrochim. Acta* 45 (1–2): 51–58.

33 Jumas, J.C., Lippens, P.E., Olivier-Fourcade, J. et al. (2006). Negative electrode composite material, production method, negative electrode and lithium-ion battery. Fr Patent 2873855, Eu *794993*, filed 28 July 2005 and issued 3 January 2008.

34 Aboulaich, A., Womes, M., Olivier-Fourcade, J. et al. (2010). Sn-0.4BPO$_4$ composite as a promising negative electrode for rechargeable lithium batteries. *Solid State Sci.* 12 (1): 65–72.

35 Conte, D.E., Mouyane, M., Jumas, J.C. et al. (2012). A combined Mössbauer spectroscopy and X-ray diffraction operando study of Sn-based composite anode materials for Li-ion accumulators. *J. Solid State Electrochem.* 16 (12): 3837–3848.

36 SONY (2005). Sony's new Nexelion hybrid Li-ion batteries to have thirty percent more capacity than conventional offering. Sony Group, News Releases, 15 February 2005. www.sony.com/en/SonyInfo/News/Press/200502/05-006E. (accessed 4 February 2023).

37 Hassoun, J., Panero, S., Mulas, G., and Scrosati, B. (2007). An electrochemical investigation of a Sn–Co–C ternary alloy as a negative electrode in Li-ion batteries. *J. Power Sources* 171 (2): 928–931.

38 Mao, O., Dunlap, R.A., and Dahn, J.R. (1999). Mechanically alloyed Sn–Fe(–C) powders as anode materials for Li-ion batteries: I. The Sn$_2$Fe–C system. *J. Electrochem. Soc.* 146 (2): 405–413.

39 Ferguson, P.P., Martine, M.L., George, A.E., and Dahn, J.R. (2009). Studies of tin–transition metal–carbon and tin–cobalt–transition metal–carbon negative electrode materials prepared by mechanical attrition. *J. Power Sources* 194 (2): 794–800.

40 Ferguson, P.P., Dunlap, R.A., and Dahn, J.R. (2010). An *in situ* study of the electrochemical reaction of Li with nanostructured $Sn_{30}Co_{30}C_{40}$. *J. Electrochem. Soc.* 157 (3): A326–A332.

41 Chamas, M., Lippens, P.E., Jumas, J.C. et al. (2011). Comparison between microparticles and nanostructured particles of $FeSn_2$ as anode materials for Li-ion batteries. *J. Power Sources* 196 (16): 7011–7015.

42 Le Caer, G., Malaman, B., Venturini, G., and Kim, I.B. (1982). [119]Sn hyperfine fields in $MnSn_2$. *Phys. Rev. B* 26 (9): 5085–5096.

43 Le Caer, G., Malaman, B., Venturini, G. et al. (1985). A Mossbauer study of $FeSn_2$. *J. Phys. F* 15 (8): 1813–1827.

44 Chamas, M., Sougrati, M.T., Reibel, C., and Lippens, P.E. (2013). Quantitative analysis of the initial restructuring step of nanostructured $FeSn_2$-based anodes for Li-ion batteries. *Chem. Mater.* 25 (12): 2410–2420.

45 Mahmoud, A., Chamas, M., Jumas, J.-C. et al. (2013). Electrochemical performances and mechanisms of $MnSn_2$ as anode material for Li-ion batteries. *J. Power Sources* 244: 246–251.

46 Philippe, B., Mahmoud, A., Ledeuil, J.B. et al. (2014). $MnSn_2$ electrodes for Li-ion batteries: mechanisms at the nano scale and electrode/electrolyte interface. *Electrochem. Acta* 123 (20): 72–83.

47 Ionica-Bousquet, C.M., Lippens, P.E., Aldon, L. et al. (2006). *In situ* [119]Sn Mössbauer effect study of Li−$CoSn_2$ electrochemical system. *Chem. Mater.* 18 (26): 6442–6447.

48 Wang, S., He, M., Walter, M. et al. (2018). Monodisperse $CoSn_2$ and $FeSn_2$ nanocrystals as high-performance anode materials for lithium-ion batteries. *Nanoscale* 10 (15): 6827–6831.

49 Ehinon, K.K.D., Naille, S., Dedryvère, R. et al. (2008). Ni_3Sn_4 electrodes for Li-ion batteries: Li−Sn alloying process and electrode/electrolyte interface phenomena. *Chem. Mater.* 20 (16): 5388–5398.

50 Naille, S., Dedryvère, R., Zitoun, D., and Lippens, P.E. (2009). Atomic-scale characterization of tin-based intermetallic anodes. *J. Power Sources* 189 (1): 806–808.

51 Naille, S., Lippens, P.E., Morato, F. et al. (2006). [119]Sn Mössbauer study of nickel–tin anodes for rechargeable lithium-ion batteries. *Hyperfine Interact.* 167 (1–3): 785–790.

52 Fransson, L., Nordström, E., Edström, K. et al. (2002). Structural transformations in lithiated η'-Cu_6Sn_5 electrodes probed by *in situ* Mössbauer spectroscopy and X-ray diffraction. *J. Electrochem. Soc.* 149 (6): A736–A742.

53 Naille, S., Dedryvère, R., Martinez, H. et al. (2007). XPS study of electrode/electrolyte interfaces of η-Cu_6Sn_5 electrodes in Li-ion batteries. *J. Power Sources* 174 (2): 1086–1090.

54 Tan, X.F., McDonald, S.D., Gu, Q. et al. (2019). Characterisation of lithium-ion battery anodes fabricated via *in-situ* Cu_6Sn_5 growth on a copper current collector. *J. Power Sources* 415 (1): 50–61.

55 Li, J. and Dahn, J.R. (2009). An *in situ* X-ray diffraction study of the reaction of Li with crystalline Si. *J. Electrochem. Soc.* 154 (3): A156–A161.

56 Edfouf, Z., Sougrati, M., Fariaut-Georges, C. et al. (2013). Reactivity assessment of lithium with the different components of novel $Si/Ni_{3.4}Sn_4/Al/C$ composite anode for Li-ion batteries. *J. Power Sources* 238 (15): 210–217.

57 Jumas, J.C., Lippens, P.E., Olivier-Fourcade, J. et al. (2017). Nouveau matériau composite enrichi en silicium, son procédé de fabrication et son utilisation à titre d'électrode. Fr Patent 3051483, filed 19 May 2017 and issued 24 November 2017.

58 Azib, T., Bibent, N., Latroche, M. et al. (2020). Ni–Sn intermetallics as efficient buffering matrix of Si anodes in Li-ion batteries. *J. Mater. Chem. A* 8 (35): 18132–18142.

59 He, Y., Ye, Z., Chamas, M. et al. (2022). Porous $Si/Cu_6Sn_5/C$ composite containing native oxides as anode material for Li-ion batteries. *J. Mater. Sci. Mater. Electron.* 33: 235–243.

60 Pahdi, A.K., Nanjundaswamy, K.S., and Goodenough, J.B. (1997). Phospho-olivines as positive-electrode materials for rechargeable lithium batteries. *J. Electrochem. Soc.* 144 (4): 1188–1194.

61 El Khalifi, M. and Lippens, P.E. (2016). First-principles investigation of the ^{57}Fe Mössbauer parameters of $LiFePO_4$ and $FePO_4$. *J. Phys. Chem. C* 120 (45): 28375–28389.

62 Andersson, A.S., Kalska, B., Häggström, L. et al. (2000). Lithium extraction/insertion in $LiFePO_4$: an X-ray diffraction and Mössbauer spectroscopy study. *Solid State Ionics* 130 (1–2): 41–52.

63 Aldon, L., Perea, A., Womes, M. et al. (2010). Determination of the Lamb-Mössbauer factors of $LiFePO_4$ and $FePO_4$ for electrochemical *in situ* and operando measurements in Li-ion batteries. *J. Solid State Chem.* 183 (1): 218–222.

64 Jumas, J.C., Sougrati, M.T., Perea, A. et al. (2013). Combined operando studies of new electrode materials for Li-ion batteries. *Hyperfine Interact.* 217 (1): 107–115.

65 Mahmoud, A., Karegeya, C., Sougrati, M.T. et al. (2018). Electrochemical mechanism and effect of carbon nanotubes on the electrochemical performance of $Fe_{1.19}(PO_4)(OH)_{0.57}(H_2O)_{0.43}$ cathode material for Li-ion batteries. *ACS Appl. Mater. Interfaces* 10 (40): 34202–34211.

66 Difi, S., Saadoune, I., Sougrati, M.T. et al. (2015). Mechanisms and performances of $Na_{1.5}Fe_{0.5}Ti_{1.5}(PO_4)_3/C$ composite as electrode material for Na-ion batteries. *J. Phys. Chem. C* 119 (45): 25220–25234.

67 Difi, S., Saadoune, I., Sougrati, M.T. et al. (2016). Role of iron in $Na_{1.5}Fe_{0.5}Ti_{1.5}(PO_4)_3/C$ as electrode material for Na-ion batteries studied by operando Mössbauer spectroscopy. *Hyperfine Interact.* 237 (1): 61–68.

68 Delmas, C., Cherkaoui, F., Nadiri, A., and Hagenmuller, P. (1987). A nasicon-type phase as intercalation electrode: $NaTi_2(PO_4)_3$. *Mater. Res. Bull.* 22 (5): 631–639.

69 Jumas, J.C., Sougrati, M.T., Olivier-Fourcade, J. et al. (2013). Identification and quantification of Sn-based species in trimetallic Pt-Sn-In/Al$_2$O$_3$-Cl naphtha-reforming catalysts. *Hyperfine Interact.* 217: 137–144.

70 Olivier-Fourcade, J., Womes, M., Jumas, J.C. et al. (2004). Investigation of redox properties of different PtSn/Al$_2$O$_3$ catalysts. *ChemPhysChem* 5 (11): 1734–1744.

71 Womes, M., Le Peltier, F., Morin, S. et al. (2007). Study of the reaction mechanisms between Sn-(n-C$_4$H$_9$)$_4$ and alumina surface sites. Application to the controlled preparation of PtSn/Al$_2$O$_3$ catalysts. *J. Mol. Catal. A Chem.* 266 (1–2): 55–64.

72 Le Peltier, F., Didillon, B., Jumas, J.C. et al. (2003). Supported bimetallic catalyst with a strong interaction between a group VIII metal and tin and its use in a catalytic reforming process. Patent FR2813209, US2002045544, EP1181978, 23 August 2001 and issues 12 August 2003.

73 Le Peltier, F., Didillon, F., Jumas, J.C. et al. (2003). Process for dehydrogenating organic compounds in the presence of a supported bimetallic catalyst with a strong interaction between a group VIII metal and tin. Patent FR2813304, US20020445787, EP1182180, filed 23 August 2001 and issues 29 July 2003.

74 Jahel, A., Avenier, P., Lacombe, S. et al. (2010). Effect of indium in trimetallic Pt/Al$_2$O$_3$SnIn–Cl naphtha-reforming catalysts. *J. Catal.* 272 (2): 275–286.

75 Jahel, A., Lacombe, S., Avenier, P. et al. (2012). Mössbauer spectroscopy: an elegant tool for the active sites identification and quantification in Pt-Sn-In based naphtha reforming catalysts. *Hyperfine Interact.* 207 (1–3): 37–40.

76 Jahel, A., Moizan-Baslé, V., Chizallet, C. et al. (2012). Effect of indium doping of γ-alumina on the stabilization of PtSn alloyed clusters prepared by surface organostannic chemistry. *J. Phys. Chem. C* 116 (18): 10073–10083.

77 Avenier, P., Lacombe, S., Jumas, J.C., Olivier-Fourcade, J. (2012). Multi-metallic catalyst with a strong metallic interaction. FR Patent 2947464, filed 15 June 2010 and issues 17 May 2012.